DocuServe

Electronic Delivery Cover Sheet

Caltech Library Services

Rapid #: -11297437

CROSS REF ID: **433804**

LENDER: **CPS :: Main Library**

BORROWER: **CIT :: Caltech Library**

TYPE:	Article CC:CCG
JOURNAL TITLE:	Finite elements in analysis and design
USER JOURNAL TITLE:	Finite Elements in Analysis and Design
ARTICLE TITLE:	Nonlinear dynamic analysis of creased shells
ARTICLE AUTHOR:	Ota, N.S.N.,
VOLUME:	121
ISSUE:	1
MONTH:	
YEAR:	2016
PAGES:	64-
ISSN:	0168-874X
OCLC #:	12178292

Processed by RapidX: 11/30/2016 11:35:56 AM

Finite Elements in Analysis and Design 121 (2016) 64–74

Contents lists available at ScienceDirect

Finite Elements in Analysis and Design

journal homepage: www.elsevier.com/locate/finel

Nonlinear dynamic analysis of creased shells

N.S.N. Ota [a,*], L. Wilson [b], A. Gay Neto [a], S. Pellegrino [b], P.M. Pimenta [a]

[a] Polytechnic School at University of São Paulo, São Paulo, Brazil
[b] Graduate Aerospace Laboratories, California Institute of Technology, 1200 E. California Blvd, Pasadena, CA 91125, United States

ARTICLE INFO

Article history:
Received 19 February 2016
Received in revised form
27 May 2016
Accepted 17 July 2016
Available online 13 August 2016

Keywords:
Shells
Dynamic analysis
Foldable curved structures
Triangular finite element

ABSTRACT

Recent studies analyze the behavior of advanced shell structures, like foldable, multistable or morphing shell structures. Simulating a thin foldable curved structure is not a trivial task: the structure may go through many snapping transitions from a stable configuration to another. Then, one could claim arc-length methods or use a dynamic approach to perform such simulations. This work presents a geometrically exact shell model for nonlinear dynamic analysis of shells. An updated Lagrangian framework is used for describing kinematics. Several numerical examples of folding a thin dome are presented, including creased shells. The triangular shell finite element used offers great flexibility for the generation of the unstructured curved meshes, as well as great results.

1. Introduction

Curved shells can be found in many natural and man-made structures. Shells have high structural efficiency due to their curvature, as bending and stretching are coupled to handle deformations, making them energetically costly to deform. Due to their high strength/weight ratio, ability to shelter inner components and a good esthetic value, shells are important structures for engineering applications. Many examples can be listed: pipes, beer cans, eggshells, skulls, bells, bowls, tents, corneas, lens, wine glasses, tanks, silos, domes, roofs, structures of airplanes, submarines, ships, rockets, missiles, etc.

The study of shells dates back to the nineteenth century, when Love [1] presented important contributions to the thin shell theory. He applied the Kirchhoff's assumptions [2], originally derived to thin plate bending theory, to the shell theory, together with the assumptions of small deflection and small thickness of the shell. Similar first order approximation shell theories were presented by Donnell [3], Sanders [4] and Flügge [5].

A second order approximation shell theory was derived by Reissner [6,7], where the assumptions on the preservation of the normals and that the transverse normal strain may be neglected were abandoned, thus considering the deformations caused by the transverse shear forces.

The geometrically nonlinear shell theory had considerable contributions by authors like Mushtari [8], Sanders [9], Naghdi and Nordgren [10], Vlasov [11], Simmonds and Danielson [12], Pimenta [13], Ibrahimbegovic [14,15] and Libai and Simmonds [16]. Formulations on nonlinear dynamic shell structures were presented by Simo et al. [17], Kuhl and Ramm [18], Brank et al. [19], Campello et al. [20], among others. Dynamic instability was analyzed by authors like Brank et al. [21] and Delaplace et al. [22]. The numerical time integration recommended therein is probably the simplest way to introduce some energy dissipation in nonlinear dynamic problems, keeping the second order accuracy of the original Newmark algorithm. We would like to compare the examples presented therein with our formulation in future works. In [20], general hyperelastic materials can be used for nonlinear dynamic analysis of shells with rotational degrees-of-freedom.

Recent studies analyze the behavior of advanced shell structures, like foldable structures [23,24] and deployable structures [25,26], structures that can be transported in a compact form and deployed to their full extent when needed, metamaterials [27,28], whose unusual properties derive from their structure, rather from their composition, morphing shell structures [29–31], shells capable of undergoing large changes in shape, whilst remaining within the material's elastic range, and multistable structures [32–34], which have more than one stable state and can move elastically from one state to another.

Following the creased hemisphere presented in [34], this paper presents a dynamic formulation for simulating that hemisphere and other similar shell structures. The presented formulation is geometrically exact for nonlinear applications involving large displacements and large rotations. We emphasize that the main novelty of present work is, contrary to our previous paper [20], the establishment of the weak form for dynamic shell models by using the symmetric Principle of Virtual Work (PVW), together with the

* Corresponding author.
E-mail addresses: nadia.ota@usp.br (N.S.N. Ota), lwilson@caltech.edu (L. Wilson), alfredo.gay@usp.br (A. Gay Neto), sergiop@caltech.edu (S. Pellegrino), ppimenta@usp.br (P.M. Pimenta).

http://dx.doi.org/10.1016/j.finel.2016.07.008
0168-874X/

update description of rotation using Rodrigues parameters. This was motivated by the objective of studying the stability of shell structures, particularly the creased-domes. For that, it is desirable to establish a weak form that can be obtained from a potential. Then, the stability assessment is more direct. We intend to make a deeper study on future works by tracking the evolution of the system natural frequencies. In this context, the Lyapunov stability criterion can be claimed, such as previously done for cable-like structures in [35]. Furthermore, when addressing the PVW to establish the weak form, the static problem becomes a particular case of dynamics, recovering the results from [20,36]. We need that to compare dynamics to statics, as performed in the present work of numerical examples.

The scope of this work is to present a numerical procedure to analyze challenging shell problems (from a numerical point of view). The triangular finite element used, the T6-3i [37], offers great flexibility for unstructured curved meshes generation and presented excellent results. The hemisphere simulations were repeated in LS-Dyna, a commercial finite element package to provide a comparison with the simulations using T6-3i elements.

2. Shell modeling

2.1. Kinematics

The shell model presented here is an extension of the geometrically exact formulation derived in [38]. The finite shell element devised in [38], the T6-3i element, is triangular, allowing robust and versatile numerical discretization. The formulation is pure-displacement based, where no mixed or hybrid types of variables were used, it is free of locking effects due to the incompatibility of the element to the rotations field, and the degrees of freedom used are simple and physically meaningful: the displacements and rotations of the shell director. The kinematics is of the Reissner–Mindlin type, which takes into account the effects of shear deformations.

In this work, the rotation tensor $\boldsymbol{Q}$ is expressed in terms of the Rodrigues rotation parameters, as in [20]. The parameterization with the Rodrigues rotation vector leads to simpler and more efficient expressions compared to the Euler parameterization, as it is totally free of trigonometric functions.

The Rodrigues rotation vector is defined by [39]:

$$\boldsymbol{\alpha} = \frac{\tan(\theta/2)}{\theta/2}\boldsymbol{\theta} \tag{1}$$

where $\boldsymbol{\theta}$ is the classical Euler rotation vector representing an arbitrary finite rotation on 3D space and $\theta = \|\boldsymbol{\theta}\|$ is its magnitude —the Euler rotation angle. The rotation tensor $\boldsymbol{Q}$ expressed in terms of the Rodrigues rotation parameter $\boldsymbol{\alpha}$ can therefore be written as [38]:

$$\boldsymbol{Q} = \boldsymbol{I} + \frac{4}{4+\alpha^2}\left(\boldsymbol{A} + \frac{1}{2}\boldsymbol{A}^2\right) \tag{2}$$

with $\alpha = \|\boldsymbol{\alpha}\|$, and $\boldsymbol{A} = skew(\boldsymbol{\alpha})$.[1]

The angular velocity operator $\boldsymbol{\Omega} = \dot{\boldsymbol{Q}}\boldsymbol{Q}^T$ is the skew-symmetric spin tensor associated to the rotation $\boldsymbol{Q}$. Its axial vector $\boldsymbol{\omega} = axial(\boldsymbol{\Omega})$ is the spin vector or angular velocity vector. Using Rodrigues parameters one can obtain:

$$\boldsymbol{\omega} = \boldsymbol{\Xi}\dot{\boldsymbol{\alpha}} \tag{3}$$

where the tensor $\boldsymbol{\Xi}$ relates $\boldsymbol{\omega}$ to the time derivative of $\boldsymbol{\alpha}$ and is given by:

$$\boldsymbol{\Xi} = \frac{4}{4+\alpha^2}\left(\boldsymbol{I} + \frac{1}{2}\boldsymbol{A}\right) \tag{4}$$

The back-rotated counterpart of $\boldsymbol{\omega}$ can be obtained by $\boldsymbol{\omega}^r = \boldsymbol{Q}^T\boldsymbol{\omega} = \boldsymbol{\Xi}^T\dot{\boldsymbol{\alpha}}$, where the notation with a superscript "r" defines back-rotated quantities. Upon time differentiating $\boldsymbol{\omega}$, one can obtain the angular acceleration vector:

$$\dot{\boldsymbol{\omega}} = \dot{\boldsymbol{\Xi}}\dot{\boldsymbol{\alpha}} + \boldsymbol{\Xi}\ddot{\boldsymbol{\alpha}} \tag{5}$$

with

$$\dot{\boldsymbol{\Xi}} = \frac{1}{2}\frac{4}{4+\alpha^2}\left[\dot{\boldsymbol{A}} - (\boldsymbol{\alpha}\cdot\dot{\boldsymbol{\alpha}})\boldsymbol{\Xi}\right] \tag{6}$$

In the parameterization with Rodrigues rotation vector, due to the definition in Eq. (1), the rotation angle must be restricted to $-\pi < \theta < \pi$. However, with an updated formulation, this is not a limitation as rotations may not exceed π within a single time increment. Using an updated-Lagrangian framework, displacements and rotations must be updated after each time-step.

Fig. 1 (adapted from [36]) shows the shell updated model. A plane shell mid-surface is assumed at the initial reference configuration. At this configuration, it is defined a local orthonormal system $\{\boldsymbol{e}_1^r, \boldsymbol{e}_2^r, \boldsymbol{e}_3^r\}$, with corresponding coordinates $\{\xi_1, \xi_2, \zeta\}$. The vectors $\boldsymbol{e}_\alpha^r$ $(\alpha = 1, 2)$ are placed on the shell mid-plane and $\boldsymbol{e}_3^r$ is normal to this plane.

In this reference configuration, the position $\boldsymbol{\xi}$ of any material point can be described by the vector field:

$$\boldsymbol{\xi} = \boldsymbol{\zeta} + \boldsymbol{a}^r \tag{7}$$

where the vector $\boldsymbol{\zeta} = \xi_\alpha \boldsymbol{e}_\alpha^r$ describes the position of points on the reference mid-surface and $\boldsymbol{a}^r = \zeta\boldsymbol{e}_3^r$ is the shell director, with $\zeta \in H = \left[-h^b, h^t\right]$ as the thickness coordinate and $h = h^b + h^t$ as the shell thickness in the reference configuration.

At instant "i", it is defined a local orthonormal system $\{\boldsymbol{e}_1^i, \boldsymbol{e}_2^i, \boldsymbol{e}_3^i\}$, with $\boldsymbol{e}_i^i = \boldsymbol{Q}\boldsymbol{e}_i^r$ (see Fig. 1), with $\boldsymbol{e}_3^i$ aligned with the director at this instant and $\boldsymbol{e}_\alpha^i$ normal to it. Note that the director is not necessarily normal to the deformed mid-surface, thus accounting for first order shear deformations. A general material point in this configuration can be described by:

$$\boldsymbol{x}^i = \boldsymbol{z}^i + \boldsymbol{a}^i \tag{8}$$

where $\boldsymbol{z}^i = \hat{\boldsymbol{z}}(\xi_\alpha)$ is the position of a material point on the middle surface and $\boldsymbol{a}^i$ is the director at this point, obtained by $\boldsymbol{a}^i = \boldsymbol{Q}\boldsymbol{a}^r$.

Similarly, the position of any material point in the configuration at instant "$i+1$", the end of the present time-step, is described by:

$$\boldsymbol{x}^{i+1} = \boldsymbol{z}^{i+1} + \boldsymbol{a}^{i+1} \tag{9}$$

Here $\boldsymbol{a}^{i+1} = \boldsymbol{Q}^\Delta\boldsymbol{a}^i$, where $\boldsymbol{Q}^\Delta$ is the tensor representing the rotation between instants "i" and "$i+1$". The index "Δ" refers to quantities relating the instants "$i+1$" and "i". As $\boldsymbol{a}^i = \zeta\boldsymbol{e}_3^i$, then, $\boldsymbol{x}^{i+1} = \boldsymbol{z}^{i+1} + \zeta\boldsymbol{Q}^\Delta\boldsymbol{e}_3^i$, and time-differentiating this expression, one can obtain the velocity vector of any material point as:

$$\dot{\boldsymbol{x}}^{i+1} = \dot{\boldsymbol{z}}^{i+1} + \zeta\dot{\boldsymbol{Q}}^\Delta\boldsymbol{e}_3^i = \dot{\boldsymbol{z}}^{i+1} + \zeta\boldsymbol{\omega}\times\boldsymbol{e}_3^{i+1} \tag{10}$$

The displacement associated with any point of the middle plane is given by vector $\boldsymbol{u}$, and can be updated by:

$$\boldsymbol{u}^{i+1} = \boldsymbol{u}^i + \boldsymbol{u}^\Delta \tag{11}$$

The rotations can be updated by [20]:

$$\boldsymbol{\alpha}^{i+1} = \frac{4}{4-\boldsymbol{\alpha}^\Delta\cdot\boldsymbol{\alpha}^i}\left(\boldsymbol{\alpha}^\Delta + \boldsymbol{\alpha}^i + \frac{1}{2}\boldsymbol{\alpha}^\Delta\times\boldsymbol{\alpha}^i\right) \tag{12}$$

where $\boldsymbol{\alpha}^\Delta$ is the rotation vector occurred from configuration "i" to "$i+1$".

[1] The $skew(\boldsymbol{v})$ function transforms a vector $\boldsymbol{v}\in\mathcal{V}_3$ in a skew-symmetric tensor $\boldsymbol{V}$, whose axial vector is $\boldsymbol{v}$. The $axial(\boldsymbol{V})$ function transforms $\boldsymbol{V}$ in its axial vector $\boldsymbol{v}$. Let two vectors $\boldsymbol{v}$, $\boldsymbol{w}$ $\in\mathcal{V}_3$, the cross product of these vectors gives $\boldsymbol{v}\times\boldsymbol{w} = \boldsymbol{V}\boldsymbol{w}$.

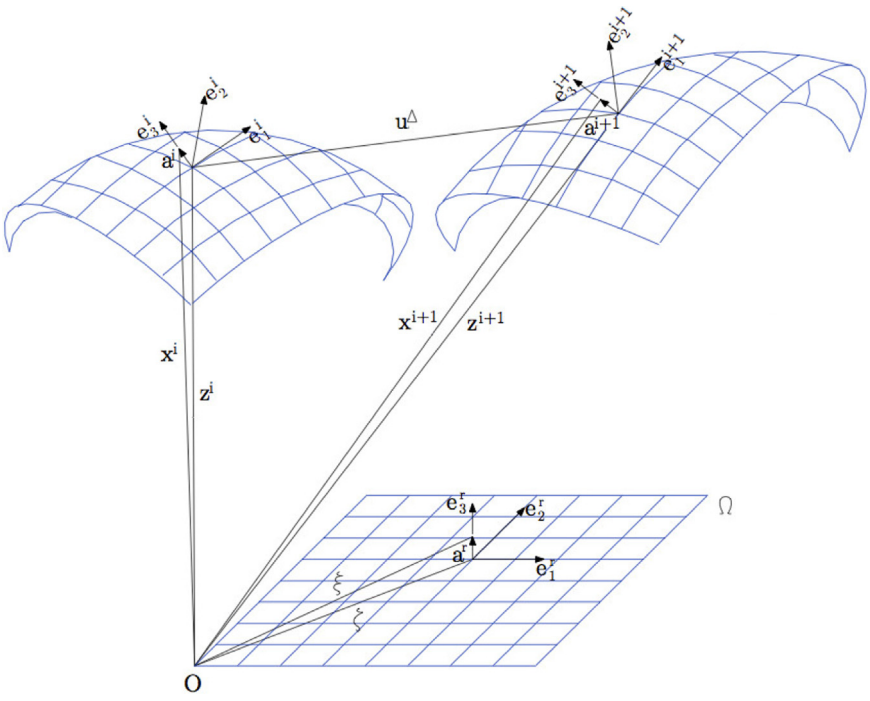

Fig. 1. Shell updated model (adapted from [36]).

2.2. Strains

The strain vectors are evaluated in the reference configuration, thus they are not affected by rigid body motion, avoiding objectivity problems. Using the notation $(\bullet)_{,\alpha}=\partial(\bullet)/\partial\xi_\alpha$ and $(\bullet)'=\partial(\bullet)/\partial\zeta$, one can define the shell strain vectors. The translational strain vector $\boldsymbol{\eta}_\alpha$ at instant "$i+1$" is given by:

$$\boldsymbol{\eta}_\alpha^{i+1}=\boldsymbol{z}_{,\alpha}^{i+1}-\boldsymbol{e}_\alpha^{i+1} \tag{13}$$

Its back-rotated counterpart is obtained by multiplying both sides of Eq. (13) by $\boldsymbol{Q}^{i+1^T}$:

$$\boldsymbol{\eta}_\alpha^{i+1^r}=\boldsymbol{Q}^{i+1^T}\boldsymbol{z}_{,\alpha}^{i+1}-\boldsymbol{e}_\alpha^{r} \tag{14}$$

In a similar way, the back-rotated specific rotation vector at instant "$i+1$" is given by:

$$\boldsymbol{\kappa}_\alpha^{i+1^r}=\boldsymbol{Q}^{i^T}\boldsymbol{\Xi}^{\Delta^T}\boldsymbol{\alpha}_{,\alpha}^{\Delta}+\boldsymbol{\kappa}_\alpha^{i^r} \tag{15}$$

with

$$\boldsymbol{\Xi}^{\Delta}=\frac{4}{4+(\boldsymbol{\alpha}^{\Delta})^2}\left(\boldsymbol{I}+\frac{1}{2}\boldsymbol{A}^{\Delta}\right) \tag{16}$$

where $\boldsymbol{A}^{\Delta}$ is the skew-symmetric tensor of $\boldsymbol{\alpha}^{\Delta}$. The generalized back-rotated strain vector for the shell model can therefore be written as:

$$\boldsymbol{\varepsilon}^{i+1^r}=\begin{bmatrix}\boldsymbol{\varepsilon}_1^{i+1^r}\\ \boldsymbol{\varepsilon}_2^{i+1^r}\end{bmatrix},\quad \text{with } \boldsymbol{\varepsilon}_\alpha^{i+1^r}=\begin{bmatrix}\boldsymbol{\eta}_\alpha^{i+1^r}\\ \boldsymbol{\kappa}_\alpha^{i+1^r}\end{bmatrix} \tag{17}$$

Upon time differentiating Eq. (17), one can obtain:

$$\dot{\boldsymbol{\varepsilon}}^{i+1^r}=\begin{bmatrix}\dot{\boldsymbol{\varepsilon}}_1^{i+1^r}\\ \dot{\boldsymbol{\varepsilon}}_2^{i+1^r}\end{bmatrix},\quad \text{with } \dot{\boldsymbol{\varepsilon}}_\alpha^{i+1^r}=\begin{bmatrix}\dot{\boldsymbol{\eta}}_\alpha^{i+1^r}\\ \dot{\boldsymbol{\kappa}}_\alpha^{i+1^r}\end{bmatrix} \tag{18}$$

that can be rewritten as:

$$\dot{\boldsymbol{\varepsilon}}_\alpha^{i+1^r}=\boldsymbol{\Lambda}^{i+1^T}\boldsymbol{\Phi}^{i+1}\boldsymbol{Y}^{\Delta}\boldsymbol{\Delta}\dot{\boldsymbol{d}}^{\Delta} \tag{19}$$

where

$$\boldsymbol{\Lambda}^{i+1}=\begin{bmatrix}\boldsymbol{Q}^{i+1} & \boldsymbol{0} & \boldsymbol{0} & \boldsymbol{0}\\ \boldsymbol{0} & \boldsymbol{Q}^{i+1} & \boldsymbol{0} & \boldsymbol{0}\\ \boldsymbol{0} & \boldsymbol{0} & \boldsymbol{Q}^{i+1} & \boldsymbol{0}\\ \boldsymbol{0} & \boldsymbol{0} & \boldsymbol{0} & \boldsymbol{Q}^{i+1}\end{bmatrix} \tag{20}$$

$$\boldsymbol{\Phi}^{i+1}=\begin{bmatrix}\boldsymbol{\Phi}_1 & \boldsymbol{0}_{6\times9}\\ \boldsymbol{0}_{6\times9} & \boldsymbol{\Phi}_2\end{bmatrix},\quad \text{with } \boldsymbol{\Phi}_\alpha=\begin{bmatrix}\boldsymbol{I} & \boldsymbol{0} & \boldsymbol{Z}_{,\alpha}^{i+1}\\ \boldsymbol{0} & \boldsymbol{I} & \boldsymbol{0}\end{bmatrix} \tag{21}$$

where $\boldsymbol{Z}^{i+1}=skew(\boldsymbol{z}^{i+1})$

$$\boldsymbol{Y}^{\Delta}=\begin{bmatrix}\boldsymbol{Y}_1^{\Delta} & \boldsymbol{0}_{9\times9}\\ \boldsymbol{0}_{9\times9} & \boldsymbol{Y}_2^{\Delta}\end{bmatrix},\quad \text{with } \boldsymbol{Y}_\alpha^{\Delta}=\begin{bmatrix}\boldsymbol{I} & \boldsymbol{0} & \boldsymbol{0}\\ \boldsymbol{0} & \boldsymbol{\Xi}^{\Delta} & \boldsymbol{\Xi}_{,\alpha}^{\Delta}\\ \boldsymbol{0} & \boldsymbol{0} & \boldsymbol{\Xi}^{\Delta}\end{bmatrix} \tag{22}$$

$$\boldsymbol{\Delta}=\begin{bmatrix}\boldsymbol{\Delta}_1\\ \boldsymbol{\Delta}_2\end{bmatrix},\quad \text{with } \boldsymbol{\Delta}_\alpha=\begin{bmatrix}\boldsymbol{I}_{\frac{\partial}{\partial\xi_\alpha}} & \boldsymbol{0}\\ \boldsymbol{0} & \boldsymbol{I}_{\frac{\partial}{\partial\xi_\alpha}}\\ \boldsymbol{0} & \boldsymbol{I}\end{bmatrix} \tag{23}$$

$$\dot{\boldsymbol{d}}^{\Delta}=\begin{bmatrix}\dot{\boldsymbol{u}}^{\Delta} & \dot{\boldsymbol{\alpha}}^{\Delta}\end{bmatrix} \tag{24}$$

2.3. Internal and external loads power

The shell internal power at instant "$i+1$" on a domain $\Omega\in\mathbb{R}^2$ can be obtained by:

$$P_{int}=\int_\Omega\boldsymbol{\sigma}^{i+1^r}\cdot\dot{\boldsymbol{\varepsilon}}^{i+1^r}d\Omega=\int_\Omega\boldsymbol{\sigma}^{i+1^r}\cdot\boldsymbol{\Lambda}^{i+1^T}\boldsymbol{\Phi}^{i+1}\boldsymbol{Y}^{\Delta}\boldsymbol{\Delta}\dot{\boldsymbol{d}}^{\Delta}d\Omega \tag{25}$$

where the generalized cross-sectional stress vector is given by:

$$\boldsymbol{\sigma}^{i+1^r}=\begin{bmatrix}\boldsymbol{\sigma}_1^{i+1^r}\\ \boldsymbol{\sigma}_2^{i+1^r}\end{bmatrix},\quad \text{with } \boldsymbol{\sigma}_\alpha^{i+1^r}=\begin{bmatrix}\boldsymbol{n}_\alpha^{i+1^r}\\ \boldsymbol{m}_\alpha^{i+1^r}\end{bmatrix} \tag{26}$$

in which $\boldsymbol{n}_\alpha^{i+1^r}$ are the back-rotated cross sectional forces and $\boldsymbol{m}_\alpha^{i+1^r}$ are the back-rotated cross sectional moments, both per unit length at instant "$i+1$". They are obtained after integration along

the shell thickness of the back-rotated stress vectors, which act on cross-sectional planes whose normals on the reference configuration are $\boldsymbol{e}_i^r$.

Defining a vector $\boldsymbol{t}$ as the surface traction per unit reference area, and $\boldsymbol{b}$ as the body force per unit reference volume, the shell external power at instant "$i+1$" is given by:

$$P_{ext} = \int_\Omega \left(\overline{\boldsymbol{q}} \cdot \dot{\boldsymbol{d}}^\Delta \right) d\Omega \tag{27}$$

in which $\overline{\boldsymbol{q}}$ is the generalized external forces vector given by:

$$\overline{\boldsymbol{q}} = \begin{bmatrix} \overline{\boldsymbol{n}} \\ \boldsymbol{\Xi}^T \overline{\boldsymbol{m}} \end{bmatrix} \tag{28}$$

where $\overline{\boldsymbol{n}} = \boldsymbol{t}^t + \boldsymbol{t}^b + \int_H \boldsymbol{b}\, d\zeta$ is the applied external forces per unit area of the middle surface in the reference configuration and $\overline{\boldsymbol{m}} = \boldsymbol{a}^t \times \boldsymbol{t}^t + \boldsymbol{a}^b \times \boldsymbol{t}^b + \int_H \boldsymbol{a} \times \boldsymbol{b}\, d\zeta$ is the vector of applied external moments per unit area.

2.4. Inertial effects

The inertial effects are derived from the shell kinetic energy T. Let V be the shell volume, the kinetic energy is given by:

$$T = \frac{1}{2} \int_V \rho \dot{\boldsymbol{x}}^{i+1} \cdot \dot{\boldsymbol{x}}^{i+1} dV \tag{29}$$

where ρ is the specific mass of the shell. Substituting Eq. (10) in (29), and knowing that $\int_V \rho \dot{\boldsymbol{z}}^{i+1} \cdot (\zeta \boldsymbol{\omega} \times \boldsymbol{e}_3^{i+1}) dV = 0$ for the particular choice of mid-surface position, assuming that $h^t = h^b = h/2$, leads to:

$$T = \frac{1}{2} h\rho \int_\Omega \dot{\boldsymbol{z}}^{i+1} \cdot \dot{\boldsymbol{z}}^{i+1} d\Omega + \frac{1}{2} \rho \frac{h^3}{12} \int_\Omega \left(\boldsymbol{\omega} \times \boldsymbol{e}_3^{i+1} \right) \cdot \left(\boldsymbol{\omega} \times \boldsymbol{e}_3^{i+1} \right) d\Omega \tag{30}$$

The kinetic energy equation can be decomposed into two components $T = T_1 + T_2$, in which:

$$T_1 = \frac{1}{2} h\rho \int_\Omega \dot{\boldsymbol{z}}^{i+1} \cdot \dot{\boldsymbol{z}}^{i+1} d\Omega \tag{31}$$

$$T_2 = \frac{1}{2} \rho \frac{h^3}{12} \int_\Omega \left(\boldsymbol{\omega} \times \boldsymbol{e}_3^{i+1} \right) \cdot \left(\boldsymbol{\omega} \times \boldsymbol{e}_3^{i+1} \right) d\Omega \tag{32}$$

Time-differentiating Eqs. (31) and (32), defining $\boldsymbol{E}_3^{i+1} = skew(\boldsymbol{e}_3^{i+1})$ and applying the equality $(\boldsymbol{\omega} \times \boldsymbol{e}_3^{i+1}) = -\boldsymbol{E}_3^{i+1} \boldsymbol{\omega}$ and Eq. (3), after some algebra one can obtain:

$$\dot{T}_1 = h\rho \int_\Omega \ddot{\boldsymbol{z}}^{i+1} \cdot \dot{\boldsymbol{z}}^{i+1} d\Omega = \rho h \int_\Omega \ddot{\boldsymbol{u}}^\Delta \cdot \dot{\boldsymbol{u}}^\Delta d\Omega \tag{33}$$

$$\dot{T}_2 = \frac{\rho h^3}{12} \int_\Omega \boldsymbol{\Xi}^T \boldsymbol{E}_3^{i+1^T} \boldsymbol{E}_3^{i+1} \dot{\boldsymbol{\omega}} \cdot \dot{\boldsymbol{\alpha}}^\Delta d\Omega + \frac{\rho h^3}{12} \int_\Omega \boldsymbol{\Xi}^T \boldsymbol{E}_3^{i+1^T} \left(\boldsymbol{\omega} \times \left(\boldsymbol{E}_3^{i+1} \boldsymbol{\omega} \right) \right) \cdot \dot{\boldsymbol{\alpha}}^\Delta d\Omega \tag{34}$$

Eq. (33) is the term contribution for translational inertia effects, and in (34), the term contribution $\boldsymbol{E}_3^{i+1^T} \boldsymbol{E}_3^{i+1} \dot{\boldsymbol{\omega}}$ describes the angular acceleration effects, and the term $\left(\boldsymbol{\omega} \times \left(\boldsymbol{E}_3^{i+1} \boldsymbol{\omega} \right) \right)$ describes the gyroscopic effects on kinetic energy.

2.5. Weak form and discretization

The weak form is here established by the Principle of Virtual Work. The shell internal and external loads virtual works, δW_{int} and δW_{ext} respectively, can be expressed by:

$$\delta W_{int} = \int_\Omega \boldsymbol{\sigma}^{i+1^r} \cdot \delta \boldsymbol{\varepsilon}^{i+1^r} d\Omega = \int_\Omega \left(\boldsymbol{\sigma}^{i+1^r} \cdot \boldsymbol{\Lambda}^{i+1^T} \boldsymbol{\Phi}^{i+1} \boldsymbol{Y}^\Delta \boldsymbol{\Delta} \delta \boldsymbol{d}^\Delta \right) d\Omega \tag{35}$$

$$\delta W_{ext} = \int_\Omega \left(\overline{\boldsymbol{q}} \cdot \delta \boldsymbol{d}^\Delta \right) d\Omega \tag{36}$$

Let δT be the virtual variation of the kinetic energy, the principle of virtual work gives:

$$\delta W_{int} - \delta W_{ext} + \delta T = 0 \tag{37}$$

where $\delta T = \delta T_1 + \delta T_2$, and

$$\delta T_1 = \rho h \int_\Omega \ddot{\boldsymbol{u}}^\Delta \cdot \delta \boldsymbol{u}^\Delta d\Omega \tag{38}$$

$$\delta T_2 = \frac{\rho h^3}{12} \int_\Omega \boldsymbol{\Xi}^T \left[\boldsymbol{E}_3^{i+1^T} \boldsymbol{E}_3^{i+1} \dot{\boldsymbol{\omega}} + \boldsymbol{E}_3^{i+1^T} \left(\boldsymbol{\omega} \times \left(\boldsymbol{E}_3^{i+1} \boldsymbol{\omega} \right) \right) \right] \cdot \delta \boldsymbol{\alpha}^\Delta d\Omega \tag{39}$$

The consistent linearization of Eq. (37) leads to the tangent operator:

$$\Delta(\delta W) = \Delta(\delta W_{int}) - \Delta(\delta W_{ext}) + \Delta(\delta T) \tag{40}$$

The components of the tangent operator $\Delta(\delta W_{int})$ and $\Delta(\delta W_{ext})$ are fully developed in [38,36]. The kinetic energy component $\Delta(\delta T)$ is an innovative contribution of this paper and is presented hereafter. The material formulation employed in this work is the same presented in [38,40].

In order to obtain the tangent operator, one needs to compute:

$$\begin{aligned} \Delta(\delta T) &= \Delta(\delta T_1) + \Delta(\delta T_2) \\ &= \rho h \int_\Omega \left(\boldsymbol{f}_{\boldsymbol{u},\boldsymbol{u}} \Delta \boldsymbol{u}^\Delta + \boldsymbol{f}_{\boldsymbol{u},\boldsymbol{\alpha}} \Delta \boldsymbol{\alpha}^\Delta \right) \cdot \delta \boldsymbol{u}^\Delta d\Omega \\ &\quad + \frac{\rho h^3}{12} \int_\Omega \left(\boldsymbol{f}_{\boldsymbol{\alpha},\boldsymbol{u}} \Delta \boldsymbol{u}^\Delta + \boldsymbol{f}_{\boldsymbol{\alpha},\boldsymbol{\alpha}} \Delta \boldsymbol{\alpha}^\Delta \right) \cdot \delta \boldsymbol{\alpha}^\Delta d\Omega \end{aligned} \tag{41}$$

with $\boldsymbol{f}_{\boldsymbol{u}} = \ddot{\boldsymbol{u}}$ and

$$\boldsymbol{f}_{\boldsymbol{\alpha}} = \boldsymbol{\Xi}^T \left[\boldsymbol{E}_3^{i+1^T} \boldsymbol{E}_3^{i+1} \dot{\boldsymbol{\omega}} + \boldsymbol{E}_3^{i+1^T} \left(\boldsymbol{\omega} \times \left(\boldsymbol{E}_3^{i+1} \boldsymbol{\omega} \right) \right) \right] \tag{42}$$

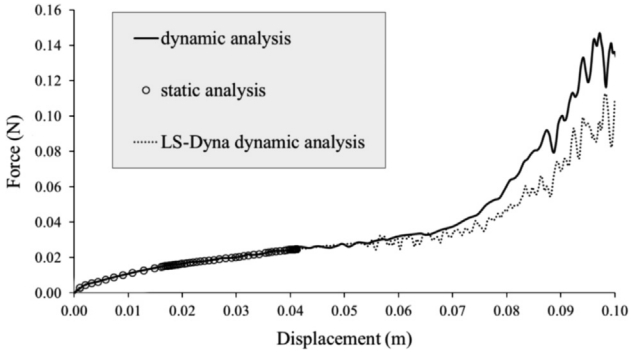

Fig. 2. Clamped dome.

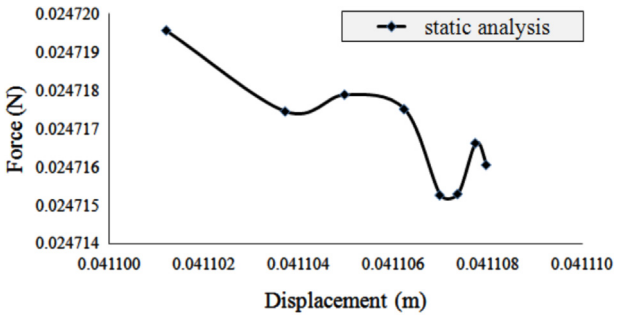

Fig. 3. Zoom: end of static analysis—clamped dome.

In matrix form:

$$\Delta(\delta T) = \begin{bmatrix} \rho h \int_\Omega \boldsymbol{N}^T \boldsymbol{f}_{\boldsymbol{u},\boldsymbol{u}} \boldsymbol{N} d\Omega & \rho h \int_\Omega \boldsymbol{N}^T \boldsymbol{f}_{\boldsymbol{u},\boldsymbol{\alpha}} \boldsymbol{N} d\Omega \\ \frac{\rho h^3}{12} \int_\Omega \boldsymbol{N}^T \boldsymbol{f}_{\boldsymbol{\alpha},\boldsymbol{u}} \boldsymbol{N} d\Omega & \frac{\rho h^3}{12} \int_\Omega \boldsymbol{N}^T \boldsymbol{f}_{\boldsymbol{\alpha},\boldsymbol{\alpha}} \boldsymbol{N} d\Omega \end{bmatrix} \begin{bmatrix} \Delta \boldsymbol{u}^\Delta \\ \Delta \boldsymbol{\alpha}^\Delta \end{bmatrix} \cdot \begin{bmatrix} \delta \boldsymbol{u}^\Delta \\ \delta \boldsymbol{\alpha}^\Delta \end{bmatrix} \tag{43}$$

where $\boldsymbol{N}$ is the shape function matrix constructed using standard Lagrange polynomials. The variables $\ddot{\boldsymbol{u}}$, $\dot{\boldsymbol{\omega}}$ and $\boldsymbol{\omega}$ are determined as functions of $\boldsymbol{u}$ and $\boldsymbol{\alpha}$ by the Newmark expressions. The Newmark method was used for time integration and the finite element method to discretize displacements and rotations in space. Let β and γ be the classical parameters from Newmark integration (in this work, it was adopted as $\beta = 0.3$ and $\gamma = 0.5$), Δt the time step and the α_1, …, α_6 coefficients given by [41]. As the damping was not the focus of this work, we kept the optimal value $\gamma = 0.5$. On the other hand, we remark here that the parameter $\beta = 0.3$ we have used in our examples has led to some energy dissipation, similar to the recommended algorithm in [21,22]. The algorithm with this value has behaved much better than with the classical value $\beta = 0.25$. Another approach would be the use of a Rayleigh type of dissipation as in [42]. We employed the integration of finite rotations presented in [43] and followed the ideas of Rodrigues parameter integration from [44]. Then:

$$\alpha_1 = \frac{1}{\beta(\Delta t)^2}, \quad \alpha_2 = \frac{1}{\beta \Delta t}, \quad \alpha_3 = \frac{1-2\beta}{2\beta}$$
$$\alpha_4 = \frac{\gamma}{\beta \Delta t}, \quad \alpha_5 = 1 - \frac{\gamma}{\beta}, \quad \alpha_6 = \left(1 - \frac{\gamma}{2\beta}\right) \Delta t \tag{44}$$

Acceleration and velocities related to configuration "$i+1$" can be written as:

$$\begin{cases} \ddot{\boldsymbol{u}}^{i+1} = \alpha_1 \boldsymbol{u}^\Delta - \alpha_2 \dot{\boldsymbol{u}}^i - \alpha_3 \ddot{\boldsymbol{u}}^i \\ \dot{\boldsymbol{u}}^{i+1} = \alpha_4 \boldsymbol{u}^\Delta + \alpha_5 \dot{\boldsymbol{u}}^i + \alpha_6 \ddot{\boldsymbol{u}}^i \end{cases} \tag{45}$$

$$\begin{cases} \boldsymbol{\omega}^{i+1} = \boldsymbol{Q}^\Delta \left(\alpha_4 \boldsymbol{\alpha}^\Delta + \alpha_5 \boldsymbol{\omega}^i + \alpha_6 \dot{\boldsymbol{\omega}}^i \right) \\ \dot{\boldsymbol{\omega}}^{i+1} = \boldsymbol{Q}^\Delta \left(\alpha_1 \boldsymbol{\alpha}^\Delta - \alpha_2 \boldsymbol{\omega}^i - \alpha_3 \dot{\boldsymbol{\omega}}^i \right) \end{cases} \tag{46}$$

In this way, the weak form is a function only of unknown generalized displacements $\boldsymbol{u}^\Delta$ and rotations $\boldsymbol{\alpha}^\Delta$, and the initial conditions for each time-step $\dot{\boldsymbol{u}}^i$, $\ddot{\boldsymbol{u}}^i$, $\boldsymbol{\omega}^i$ and $\dot{\boldsymbol{\omega}}^i$.

The symbolic evaluation of the functions $\boldsymbol{f}_{\boldsymbol{u},\boldsymbol{u}}$, $\boldsymbol{f}_{\boldsymbol{u},\boldsymbol{\alpha}}$, $\boldsymbol{f}_{\boldsymbol{\alpha},\boldsymbol{u}}$ and $\boldsymbol{f}_{\boldsymbol{\alpha},\boldsymbol{\alpha}}$ was performed using *Mathematica*® and *AceGen*® (see [45,46]).

The spatial discretization was done using the t6-3i finite element [37], a six-node element, with linear shape functions for interpolation of the rotation field related to the mid-side nodes of the triangle only and quadratic shape functions for interpolation of the displacement field. Let $\boldsymbol{p}^\Delta$ be a six-dimensional vector associated with each node, containing both displacements and rotations, the finite element approximation is given by:

$$\boldsymbol{d}^\Delta = \boldsymbol{N} \boldsymbol{p}^\Delta \tag{47}$$

where

$$\boldsymbol{d}^\Delta = \begin{bmatrix} \boldsymbol{u}^\Delta \\ \boldsymbol{\alpha}^\Delta \end{bmatrix} \tag{48}$$

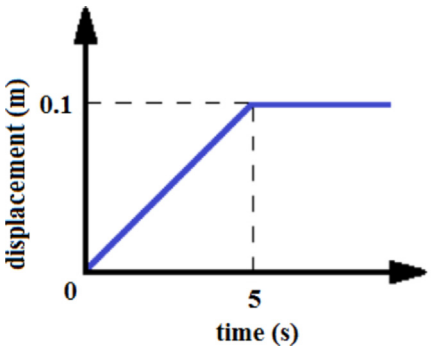

Fig. 4. Prescribed displacement variation with time.

2.6. Comparison FEA solver

The commercial finite element package, LS-Dyna, was used as a comparison explicit solver. Meshes were generated from a mixture

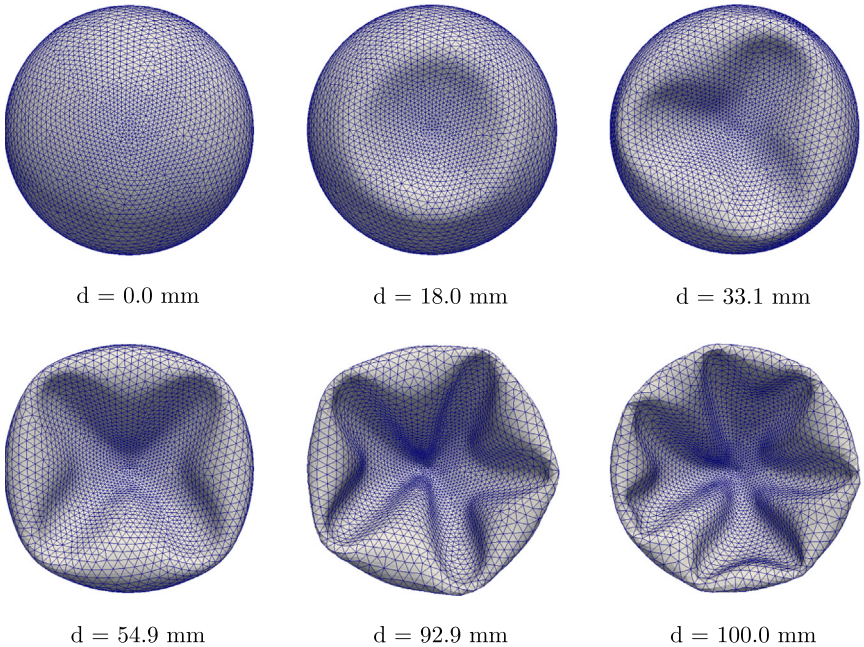

Fig. 5. Clamped dome (top view).

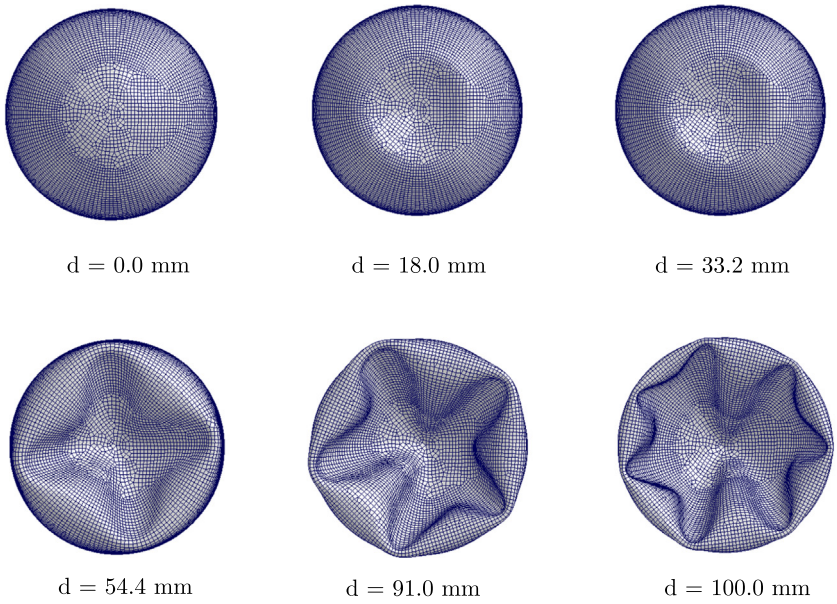

Fig. 6. LS-Dyna simulation of clamped dome (top view).

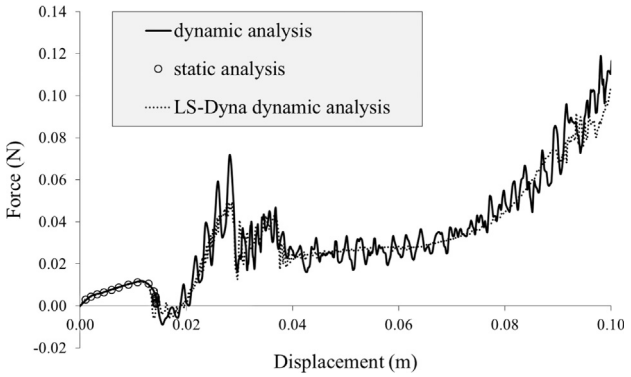

Fig. 7. Clamped dome with curved crease at $\phi = 0.6$.

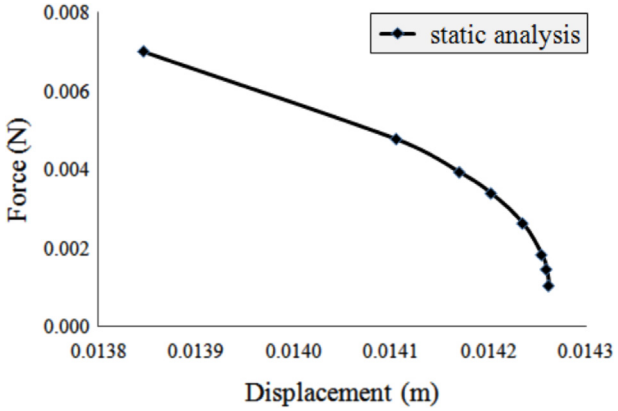

Fig. 8. Zoom: end of static analysis—clamped dome with curved crease at $\phi = 0.6$.

of quadrilateral Belytschko–Tsay and triangular C^0 shell elements. The shell element nodes have six degrees of freedom (displacements and rotations) and two through thickness integration points. The Belytschko–Tsay shell element is based on a combined co-rotational and velocity-strain formulation [47]. To avoid distortion of the quadrilateral elements, Flanagan–Belytschko hourglass integration was enabled.

In the case considered in Section 3.2 a crease needs to be incorporated into the shell surface. There are several ways creases can be formulated in LS-Dyna. One is to start with an initially kinked surface [48]. This approach has also been used to model the interaction between creases with wrinkles [49]. The crease stiffness, or the bending moment as a function of crease angle depends on the initial kink angle.

In the scenarios considered here, the creases have substantially lower bending stiffness compared to the surrounding material. To formulate the creases required in Section 3.2 the displacement degrees of freedom of the nodes on one side of the crease are tied to the elements on the other side of the crease. The rotational degrees of freedom are left unconstrained, forming a zero-stiffness crease.

3. Numerical examples

The formulation presented in this work was implemented in the finite element code Giraffe (Generic Interface Readily Accessible for Finite Elements) [50], developed at Polytechnic School at University of São Paulo, Brazil. Giraffe is a finite element interface in which it has already implemented a beam model [51] and beam to beam contact models [52].

3.1. Clamped dome

The dome, a hollow upper half of a sphere, is fully clamped in its base. The radius of the dome is 50 mm and its thickness is 1 mm. The elasticity constants for the polyvinyl siloxane material are adopted as $E = 100\ \mathrm{kN/m^2}$ (Young's modulus) and $\nu = 0.499$ (Poisson's ratio). It used an unstructured mesh of 4632 triangular six-nodes elements, 9329 nodes, with six degrees of freedom (displacements and rotations) per mid-node and three degrees of freedom (displacements) per corner-node.

A comparison LS-Dyna simulation with the same geometry and boundary conditions was performed using a mesh containing 5487 triangular C^0 and quadrilateral Belytschko–Tsay shell elements. The corresponding 5541 nodes have the six degrees of freedom (displacements and rotations).

The top of the hemisphere is pushed down in a displacement-controlled manner and the reactive force follows. The simulation

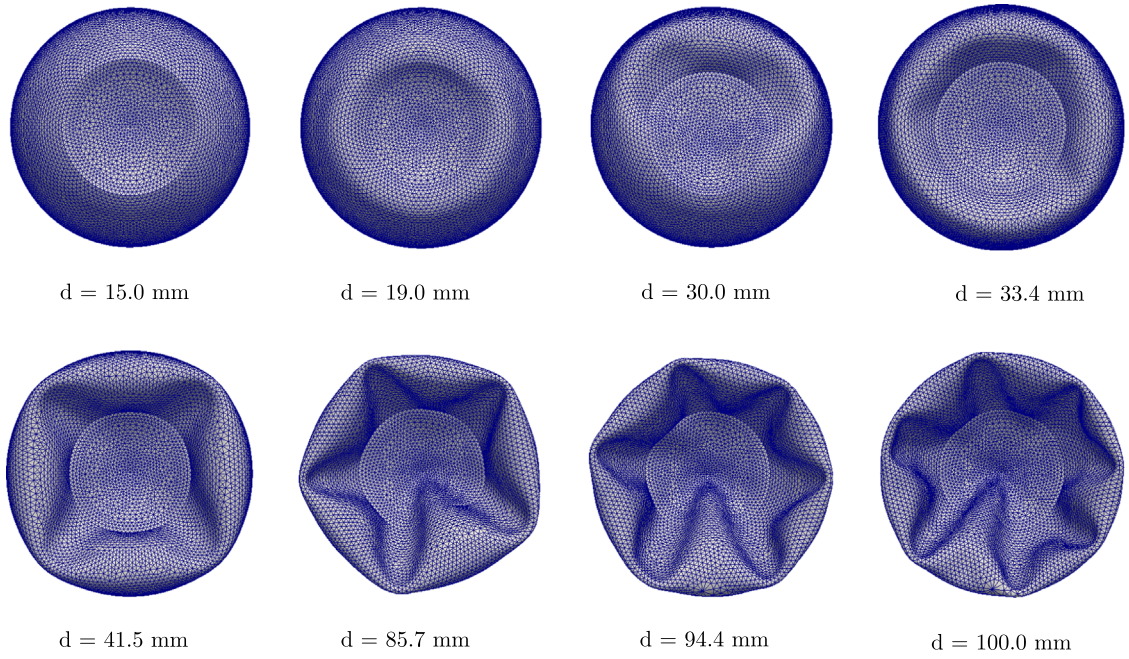

Fig. 9. Clamped dome with curved crease at $\phi = 0.6$.

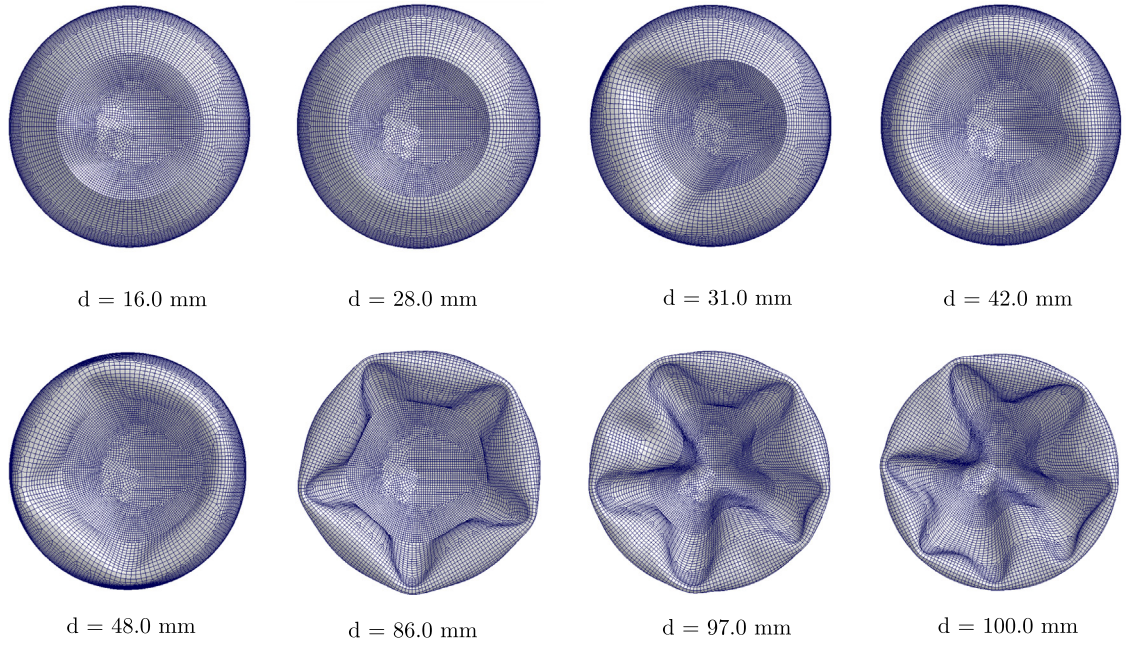

Fig. 10. LS-Dyna simulation of clamped dome with curved crease at $\phi = 0.6$.

presents various snap-throughs and snap-backs, and the static simulation cannot converge much farther since we did not employ arc-length methods, the last converged point is at displacement equal to $d = 41.1$ mm, a snap-back, as can be seen in Figs. 2 and 3. To pass through this point, a dynamic formulation was employed. Our simulation has shown a slightly stiffer behavior. We have observed along our simulations that finer meshes reduce this stiffening, which is mainly due to the strong curvatures within an element.

Fig. 4 shows the prescribed displacement used in the dynamic analysis. The displacement varies linearly from zero to 100 mm in 5 s. This time scale was chosen such that there were no relevant dynamic effects in the static analysis of the problem, leading to a quasi-static behavior. When the snap-throughs and snap-backs occur, the dynamic effects play a role.

Fig. 5 shows the dome behavior from a top view. The shape of the indented structure presents several transitions. First the indentation is circular, then it has three lobes. At the instant the top is at the height of the dome base, it presents four lobes. Towards the end of the simulation it transitions to five lobes, then six and ends with seven lobes.

Fig. 6 shows the predicted dome behavior in LS-Dyna. The lobe formation is almost identical to that of the previous simulation. The force predicted by the LS-Dyna simulation is also close up until $d = 66$ mm, after which it predicts a lower force as seen in Fig. 4. This difference is due to the more refined mesh used in the

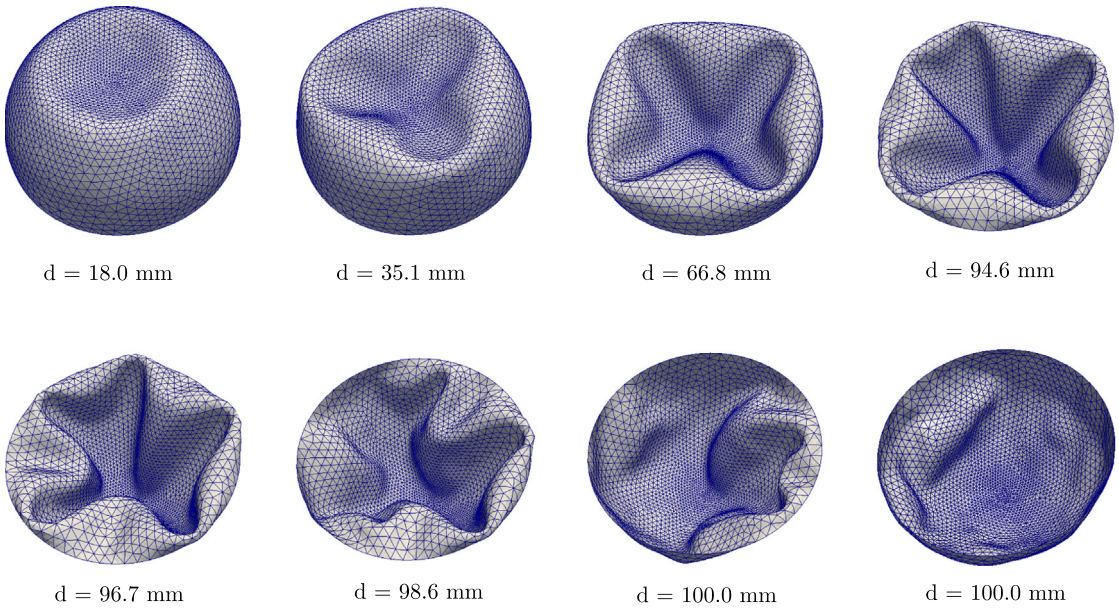

Fig. 11. Dome turning inside out.

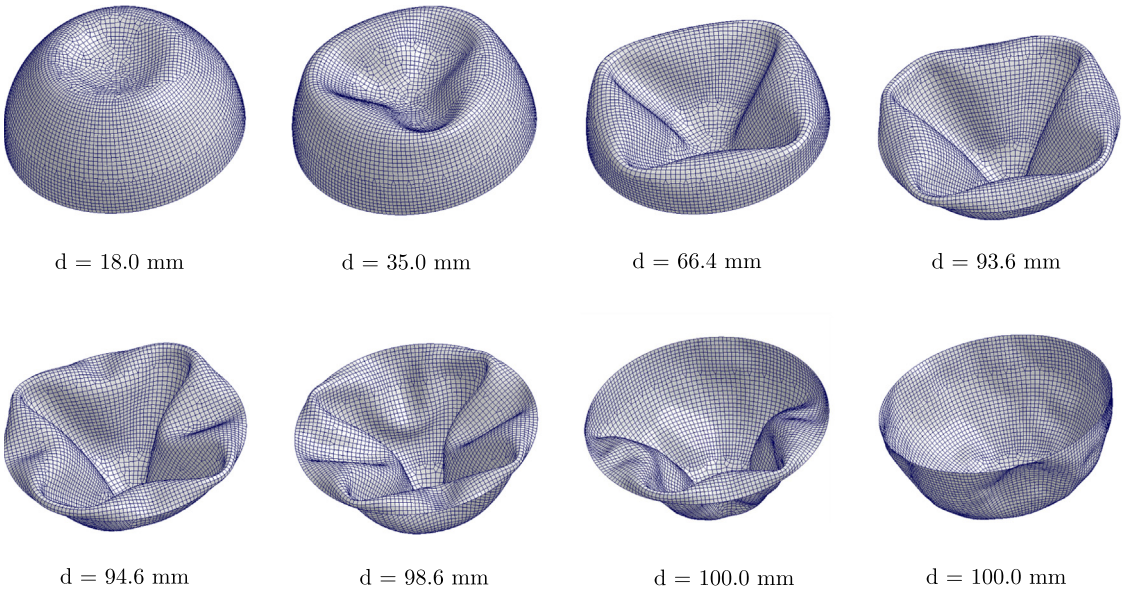

Fig. 12. LS-Dyna simulation of dome turning inside out.

LS-Dyna simulation. The more the mesh is refined, the more flexible the model.

3.2. *Clamped dome with curved crease at $\phi = 0.6$*

A dome with the same dimensions and material of the hemisphere of Section 3.1 has a curved crease parallel to the hemisphere base, as in [34]. The crease was modeled such that its nodes present only coupled displacements, but independent rotations (free). The crease distance from the dome base is obtained through the ϕ number, which relates the dome radius to the crease radius through the equation:

$$\phi = \frac{R_t}{R_s} \tag{49}$$

where R_t is the curved crease radius and R_s is the dome radius. In this example, $\phi = 0.6$, therefore, the crease radius is $R_t = 30$ mm and its distance from the base is 40 mm. It used an unstructured mesh of 9082 triangular six-nodes elements, 18,517 nodes, with six degrees of freedom (displacements and rotations) per mid-node and three degrees of freedom (displacements) per corner-node. In Fig. 7 the force profile is shown. The static formulation diverges at displacement $d = 14.2$ mm, a snap-back (Fig. 8). After this point, the force becomes negative until displacement $d = 19.0$ mm, when the indentation is still circular. The force increases reaching its maximum of $F = 0.071$ N at displacement $d = 28.2$ mm. The indented shape "falls" to the side, there appearing two lobes and the force drops to $F = 0.016$ N. These two lobes spread out in an almost-circular shape before it transitions to four lobes. Towards the end of the simulation, it transitions to five, six and seven lobes. Fig. 9 presents the dome deformation sequence.

The LS-Dyna simulations show very similar behavior in both the force profile and the deformed geometry during the simulation (Fig. 10). A mesh containing 9694 nodes and 8933 triangular C^0 and quadrilateral Belytschko–Tsay shell elements was used. In this simulation snap-through occurs slightly earlier at $d = 14.0$ mm. The

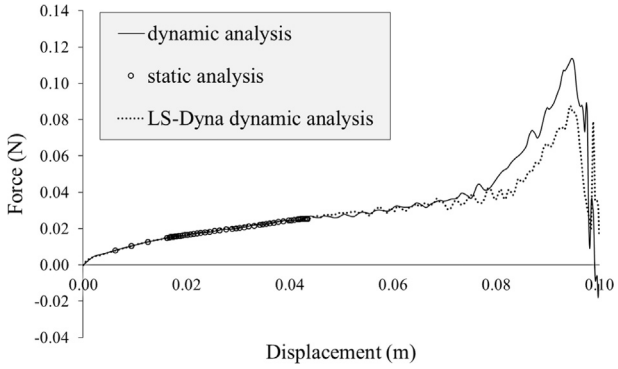

Fig. 13. Dome turning inside out.

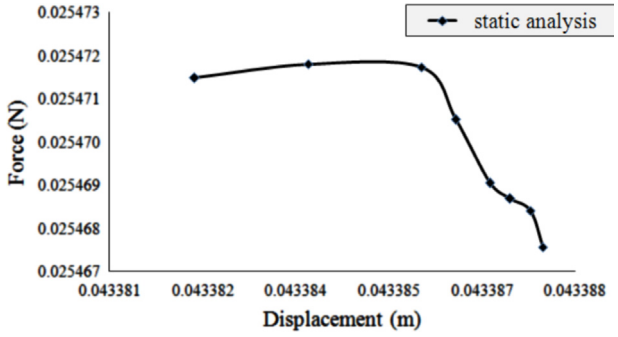

Fig. 14. Zoom: end of static analysis—dome turning inside out.

force results are less noisy after the snap-through, which gives a lower maximum force of $F=0.049$ N at displacement $d=28.6$ mm. After this, the indented shape transitions to two and then to three lobes. The shape then transitions directly to five lobes at $d=48.5$ mm. As captured in the previous simulation, towards the end of the simulation six and finally seven lobes form. The lobe transitions do occur slightly later than in the previous simulation.

3.3. Dome turning inside out

In order to analyze the case of a dome turning inside out, all rotations at the dome base were set free and the displacements were locked, like the joint used to model the crease in Section 3.2, as if the number $\phi = 1$. It used an unstructured mesh of 4632

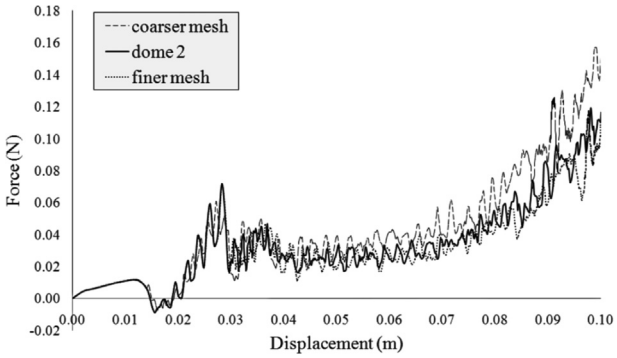

Fig. 18. Mesh discretization—creased dome.

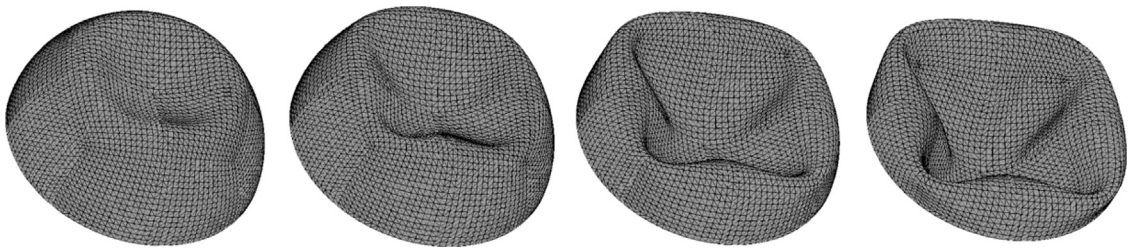

Fig. 15. Structured mesh.

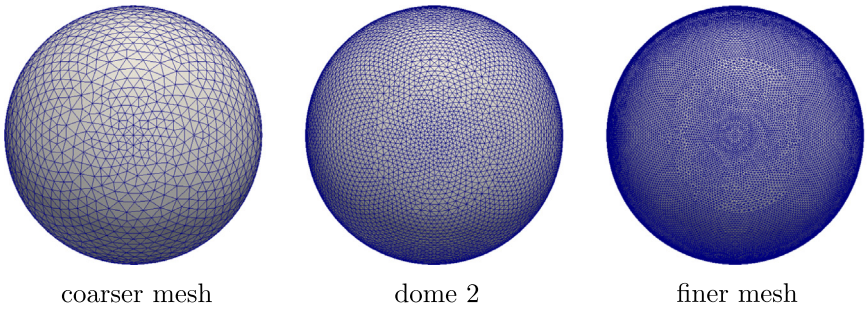

Fig. 16. Mesh discretization—creased dome—initial step.

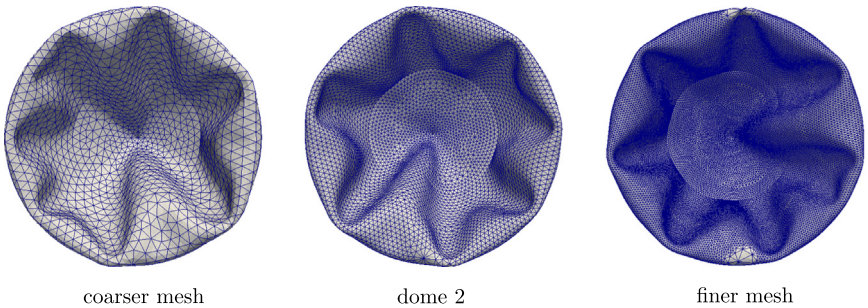

Fig. 17. Mesh discretization—creased dome—final step.

triangular six-nodes elements, 9329 nodes, with six degrees of freedom (displacements and rotations) per mid-node and three degrees of freedom (displacements) per corner-node. The deformation sequence is shown in Fig. 11, it is similar to the case in Section 3.1 until it starts to turn inside out towards the end of the simulation, the number of lobes stops increasing and the existing lobes spread out, reaching the upside down hemisphere shape. In Fig. 13, the force profile is plotted. The static formulation diverges at displacement $d=43.4$ mm (Fig. 14). By the time the hemisphere starts to turn inside out, at the displacement of $d=94.6$ mm, the force, that reached its maximum of $F=0.114$ N, starts to drop drastically, becoming negative when the dome is completely inside out.

The mesh in this LS-Dyna simulation contained 5541 nodes, 5487 triangular C^0 and quadrilateral Belytschko–Tsay shell elements. The LS-Dyna simulation shows very similar behavior in deformed geometry as seen in Fig. 12, but predicts a lower force after $d=0.076$ mm. The peak force predicted is $F=0.0866$ N at $d=94.4$ mm before dropping off sharply.

3.4. Remarks

In this section, a couple remarks about the simulations are presented: the need for an unstructured mesh and the influence of mesh refinement.

Fig. 15 presents the dome of Section 3.1 with a structured mesh. As can be seen, the mesh influences the dome indented shape. From beginning to the end of the simulation it presents always four lobes, following the symmetry of the mesh.

An unstructured mesh however does not create a point exactly at the top of the dome. This was achieved by creating a tiny region at the top of the dome with a structured mesh, in such a way that a node would be created exactly at the top of the dome, and the rest of the dome was freely meshed.

Fig. 16 shows the mesh of the dome of Section 3.2, “dome 2”, with 9082 elements and 18,517 nodes. A coarser mesh of the same dome with 2208 elements and 4593 nodes, and a finer mesh with 36,570 elements and 73,845 nodes were solved in order to analyze the effect of mesh refinement. The mesh influences the shape and position of the lobes. The number of lobes, however, does not depend on mesh refinement as can be seen in Fig. 17. In Fig. 18, the force profile is shown. For a coarser mesh, a higher force is needed, as well as a finer mesh needs lower force to the same displacement.

4. Conclusions

A geometrically exact shell model for nonlinear shell dynamic analysis was derived in this paper. The shell formulation considers an updated Lagrangian framework, allowing large rotations. The rotation field was described using the Rodrigues rotation vector, which leads to an extremely simple way to update the rotational variables. The shell kinematical model is simple and consistent. The weak form was obtained by means of the principle of virtual work. The purely displacement based triangular finite element used allows robust and versatile discretization, leading to a simple generation of the unstructured meshes in the simulations here analyzed, and working in the fully nonlinear regime in static and dynamic applications, without using any possibly expensive techniques such as ANS, EAS or hourglass control. Validity and robustness of the formulation were shown in the numerical simulations, which presented very good performance in the analyzed cases. In particular, the shell model was able to capture the snapping behavior of a hemisphere with a circular crease. The corresponding forces and deformed configurations also closely matched that of the LS-Dyna simulations used as a comparison. This model discussed herein presents great results and flexibility for analyzing the high nonlinear shell problems that take place in recent shell studies.

Acknowledgments

The first author acknowledges her Masters degree scholarship by CAPES (Coordenação de Aperfeiçoamento de Pessoal de Nível Superior). The third author acknowledges the support by CNPq (Conselho Nacional de Desenvolvimento Científico e Tecnológico) under the grant 308190/2015-7. The fifth author expresses his acknowledgement to the Alexander von Humboldt Foundation for the Georg Forster Award that made possible his stay at the Universities of Duisburg-Essen and Hannover in Germany as well as to the French and Brazilian Governments for the Chair CAPES-Sorbonne that made possible his stay at Sorbonne Universités during the year of 2016 on leave from the University of São Paulo.

References

[1] A.E.H. Love, On the small free vibrations and deformations of elastic shells, Phil. Trans. R. Soc. Lond. 179 (1888) 491–546.
[2] G.R. Kirchhoff, Über das gleichgewicht und die bewegung einer elastischen scheibe, J. reine angew. Math. 40 (1850) 51–88.
[3] L.H. Donnell, Stability of thin-walled tubes under torsion (no. naca-r-479), Technical report, California Institute of Technology, Pasadena, USA, 1933.
[4] J.L. Sanders Jr., An improved first-approximation theory for thin shells (nasa tr-r24), US Government Printing Office, Washington, DC.
[5] W. Flügge, Stresses in Shells, 1960, Springer-Verlag Berlin Heidelberg. eBook ISBN: 978-3-662-01028-0. http://dx.doi.org/10.1007/978-3-662-01028-0.
[6] E. Reissner, On the Theory of Thin Elastic Shells, JW Edwards, Ann Arbor, Michigan, 1949.
[7] E. Reissner, Stress strain relations in the theory of thin elastic shells, J. Math. Phys. 31 (1) (1952) 109–119.
[8] K.M. Mushtari, K.Z. Galimov, Non-linear theory of thin elastic shells, no. 62, Published for the National Science Foundation by the Israel Program for the Scientific Translations; available from the Office of Technical Services, US Department of Commerce, 1961.
[9] J.L. Sanders Jr., Nonlinear theories for thin shells (no. tr10), Technical report, DTIC Document, 1961.
[10] P.M. Naghdi, R.P. Nordgren, On the nonlinear theory of elastic shells under the kirchhoff hypothesis (no. tr17), Technical report, DTIC Document, 1962.
[11] V.Z. Vlasov, General Theory of Shells and its Applications in Engineering, vol. 99, National Aeronautics and Space Administration, 1964.
[12] J.G. Simmonds, D.A. Danielson, Nonlinear shell theory with finite rotation and stress-function vectors, J. Appl. Mech. 39 (4) (1972) 1085–1090.
[13] P.M. Pimenta, On a geometrically-exact finite-strain shell model, in: Proceeding of the third Pan-American Congress on Applied Mechanics, PACAM III, Escola Politécnica da Universidade de São Paulo, Brazil, 1993, pp. 616–619.
[14] A. Ibrahimbegovic, Stress resultant geometrically exact shell theory for finite rotations and its finite element implementation, Appl. Mech. Rev. 50 (4) (1997) 199–226.
[15] A. Ibrahimbegovic, B. Brank, P. Courtois, Stress resultant geometrically exact form of classical shell model and vector-like parameterization of constrained finite rotations, Int. J. Numer. Methods Eng. 52 (11) (2001) 1235–1252.
[16] A. Libai, J.G. Simmonds, The Nonlinear Theory of Elastic Shells, 2nd ed., Cambridge University Press, USA, 2005,, ISBN: 9780521019767.
[17] J.C. Simo, M.S. Rifai, D.D. Fox, On a stress resultant geometrically exact shell model. part vi: conserving algorithms for non-linear dynamics, Int. J. Numer. Methods Eng. 34 (1) (1992) 117–164.
[18] D. Kuhl, E. Ramm, Constraint energy momentum algorithm and its application to non-linear dynamics of shells, Comput. Methods Appl. Mech. Eng. 136 (3) (1996) 293–315.
[19] B. Brank, L. Briseghella, N. Tonello, F.B. Damjanic, On non-linear dynamics of shells: implementation of energy-momentum conserving algorithm for a finite rotation shell model, Int. J. Numer. Methods Eng. 42 (3) (1998) 409–442.
[20] E.M.B. Campello, P.M. Pimenta, P. Wriggers, An exact conserving algorithm for nonlinear dynamics with rotational dofs and general hyperelasticity. part 2: shells, Comput. Mech. 48 (2) (2011) 195–211.
[21] B. Brank, J. Korelc, A. Ibrahimbegović, Dynamics and time-stepping schemes for elastic shells undergoing finite rotations, Comput. Struct. 81 (12) (2003) 1193–1210.
[22] A. Delaplace, A. Ibrahimbegovic, Performance of time-stepping schemes for discrete models in fracture dynamic analysis, Int. J. Numer. Methods Eng. 65 (9) (2006) 1527–1544.

[23] M. Trautz, R. Herkrath, The application of folded plate principles on spatial structures with regular, irregular and free-form geometries, in: Symposium of the International Association for Shell and Spatial Structures (50th, 2009, Valencia). Evolution and Trends in Design, Analysis and Construction of Shell and Spatial Structures: Proceedings, Editorial Universitat Politècnica de València, 2009.
[24] T. Tachi, Freeform rigid-foldable structure using bidirectionally flat-foldable planar quadrilateral mesh, Adv. Architect. Geom. 2010 (2010) 87–102.
[25] E. Kebadze, S.D. Guest, S. Pellegrino, Bistable prestressed shell structures, Int. J. Solids Struct. 41 (11) (2004) 2801–2820.
[26] J. Block, M. Straubel, M. Wiedemann, Ultralight deployable booms for solar sails and other large gossamer structures in space, Acta Astronautica 68 (7) (2011) 984–992.
[27] J.L. Silverberg, A.A. Evans, L. McLeod, R.C. Hayward, T. Hull, C.D. Santangelo, I. Cohen, Using origami design principles to fold reprogrammable mechanical metamaterials, Science 345 (6197) (2014) 647–650.
[28] B. Florijn, C. Coulais, M. van Hecke, Programmable mechanical metamaterials, Phys. Rev. Lett. 113 (17) (2014) 175503.
[29] A. Pirrera, D. Avitabile, P.M. Weaver, Bistable plates for morphing structures: a refined analytical approach with high-order polynomials, Int. J. Solids Struct. 47 (25) (2010) 3412–3425.
[30] N. Hu, et al., Buckling-induced smart applications: recent advances and trends, Smart Mater. Struct. 24 (6) (2015) 063001.
[31] E. Lamacchia, A. Pirrera, I.V. Chenchiah, P.M. Weaver, Morphing shell structures: a generalised modelling approach, Compos. Struct. 131 (2015) 1017–1027.
[32] F. Mattioni, A. Gatto, P.M. Weaver, M.I. Friswell, K.D. Potter, The application of residual stress tailoring of snap-through composites for variable sweep wings, in: Proceedings of the 47th AIAA/ASME/ASCE/AHS/ASC Structures, Structural Dynamics, and Materials Conference, SDM, 2006.
[33] D.P. Holmes, A.J. Crosby, Snapping surfaces, Adv. Mater. 19 (21) (2007) 3589–3593.
[34] N.P. Bende, A.A. Evans, S. Innes-Gold, L.A. Marin, I. Cohen, R.C. Hayward, C. D. Santangelo, Geometrically controlled snapping transitions in shells with curved creases, Proc. Natl Acad. Sci. USA 112 (36) (2015) 11175–11180.
[35] A. Gay Neto, C.A. Martins, Structural stability of flexible lines in catenary configuration under torsion, Mar. Struct. 34 (2013) 16–40.
[36] M.L.T. Moreira, Rotation parameterization in rod and shell theories (in Portuguese), Ph.D. thesis, Universidade de São Paulo, 2009.
[37] P.M. Pimenta, E.M.B. Campello, A.G. Neto, N.S.N. Ota, A simple, robust and versatile shell finite element, IACM Expressions 38 (2016) 18–22.
[38] E.M.B. Campello, P.M. Pimenta, P. Wriggers, A triangular finite shell element based on a fully nonlinear shell formulation, Comput. Mech. 31 (6) (2003) 505–518.
[39] P.M. Pimenta, E.M.B. Campello, Geometrically nonlinear analysis of thin-walled space frames, in: Proceedings of the Second European Conference on Computational Mechanics, II ECCM, Cracow, Poland, 2001.
[40] C. Tiago, Meshless methods: extending the linear formulation and its generalization to geometrically exact structural analysis, Ph.D. thesis, Instituto Superior Técnico da Universidade Técnica de Lisboa, 2007.
[41] P. Wriggers, Nonlinear Finite Element Methods, 2008, Springer-Verlag Berlin Heidelberg. eBook ISBN: 978-3-540-71001-1. http://dx.doi.org/10.1007/978-3-540-71001-1.
[42] S. Mamouri, E. Mourid, A. Ibrahimbegovic, Study of geometric non-linear instability of 2D frame structures, Eur. J. Comput. Mech. 24 (6) (2015) 256–278, http://dx.doi.org/10.1080/17797179.2016.1181028.
[43] A. Ibrahimbegović, M.A. Mikdad, Finite rotations in dynamics of beams and implicit time-stepping schemes, Int. J. Numer. Methods Eng. 41 (5) (1998) 781–814.
[44] P.M. Pimenta, E.M.B. Campello, P. Wriggers, An exact conserving algorithm for nonlinear dynamics with rotational dofs and general hyperelasticity. Part 1: rods, Comput. Mech. 42 (5) (2008) 715–732.
[45] J. Korelc, Multi-language and multi-environment generation of nonlinear finite element codes, Eng. Comput. 18 (4) (2002) 312–327.
[46] J. Korelc, Automatic generation of finite-element code by simultaneous optimization of expressions, Theor. Comput. Sci. 187 (1) (1997) 231–248.
[47] J. Hallquist, Ls-dyna Theory Manual, Livermore Software Technology Corporation, LSTC, March, 2006.
[48] A. Papa, S. Pellegrino, Systematically creased thin-film membrane structures, J. Spacecr. Rockets 45 (1) (2008) 10–18.
[49] K. Woo, C.H. Jenkins, Analysis of crease-wrinkle interaction for thin sheets, J. Mech. Sci. Technol. 26 (3) (2012) 905–916.
[50] A. Gay Neto, Giraffe (Generic interface readily accessible for finite elements) user's manual, University of São Paulo,Brazil, v.1.0.100, Available at 〈sites.poli.usp.br/p/alfredo.gay〉.
[51] A. Gay Neto, C.A. Martins, P.M. Pimenta, Static analysis of offshore risers with a geometrically-exact 3d beam model subjected to unilateral contact, Comput. Mech. 53 (1) (2014) 125–145.
[52] A. Gay Neto, P.M. Pimenta, P. Wriggers, A master-surface to master-surface formulation for beam to beam contact, Part I: frictionless interaction, Comput. Methods Appl. Mech. Eng. 303 (2016) 400–429, http://dx.doi.org/10.1016/j.cma.2016.02.005.